

Self-gravitating planetary envelopes and the core-nucleated instability

William Béthune¹★,

¹ *Department of Applied Mathematics and Theoretical Physics, University of Cambridge, Centre for Mathematical Sciences, Wilberforce Road, Cambridge CB3 0WA, UK.*

Accepted XXX. Received YYY; in original form ZZZ

ABSTRACT

Planet formation scenarios can be constrained by the ratio of the gaseous envelope mass relative to the solid core mass in the observed exoplanet populations. One-dimensional calculations find a critical (maximal) core mass for quasi-static envelopes to exist, suggesting that envelopes around more massive cores should collapse due to a ‘core-nucleated’ instability. We study self-gravitating planetary envelopes via hydrodynamic simulations, progressively increasing the dimensionality of the problem. We characterize the core-nucleated instability and its non-linear evolution into runaway gas accretion in one-dimensional spherical envelopes. We show that rotationally-supported envelopes can enter a runaway accretion regime via polar shocks in a two-dimensional axisymmetric model. This picture remains valid for high-mass cores in three dimensions, where the gas gravity mainly adds up to the core gravity and enhances the mass accretion rate of the planet in time. We relate the core-nucleated instability to the absence of equilibrium connecting the planet to its parent disk and discuss its relevance for massive planet formation.

Key words: planets and satellites: gaseous planets, formation – hydrodynamics – instabilities – methods: numerical

1 INTRODUCTION

In the common picture of giant planet formation, a gravitational instability (GI) triggers the collapse of gas clumps into protoplanets (Podolak et al. 1993). The disk instability scenario relies on the GI of massive and cold circumstellar disks (Safronov 1960; Toomre 1964). This GI can lead to the fragmentation of the disk into substellar companions (Boss 1998, 2000), provided an efficient radiative cooling (Gammie 2001; Rice et al. 2003; Booth & Clarke 2019). While disks around class 0/I protostars might be massive enough (e.g., Eisner et al. 2005; ALMA Partnership et al. 2015; Liu et al. 2016), unambiguous signatures of their GI are still looked for (Dong et al. 2016; Forgan et al. 2016, 2018).

Alternatively, planets may grow embedded in the disk (Safronov 1969; Goldreich & Ward 1973), accumulating dust grains into Earth-sized planetary cores (e.g., Birnstiel et al. 2016; Nimmo et al. 2018). As the solid core grows more massive, it attracts more of the surrounding gas in a dense envelope — its primordial atmosphere (Pollack et al. 1996). In this core-accretion scenario, planetary envelopes become prone to a GI when massive enough (Cameron 1973), pro-

viding a way to form gas giants within gravitationally stable disks (Lissauer & Stevenson 2007).

Looking for spherically-symmetric envelope equilibria, Perri & Cameron (1974) found no solution beyond a *critical core mass*. For a core mass smaller than this critical value, they found two possible solutions for the envelope, and the most massive solution was generally unstable. Since no stable equilibrium can be found beyond the critical mass, the envelope is expected to contract and start accreting gas in a runaway fashion, transforming massive cores into gas giants via the core-nucleated instability.

Subsequent studies aimed at deriving more realistic estimates for the critical core mass. Different assumptions were made regarding the energy transport through the envelope (Mizuno et al. 1978; Hayashi et al. 1979; Mizuno 1980; Sasaki 1989), the grain opacity and accretion luminosity onto the core (Ikoma et al. 2001; Rafikov 2006). In time dependent models, runaway gas accretion starts when the accretion luminosity can no longer balance the radiative cooling and contraction of the envelope (Pollack et al. 1996; Ikoma et al. 2000). However, these studies always considered the envelope as one-dimensional and quasi-static.

Wuchterl (1991a,b) presented the first hydrodynamic calculations of one-dimensional gravitating envelopes. At the

★ E-mail: wb288@damtp.cam.ac.uk

critical core mass, [Wuchterl \(1991b\)](#) reported a departure from thermal and hydrostatic equilibrium leading to the *ejection* of the envelope. Using three-dimensional hydrodynamic simulations, [Ayliffe et al. \(2012\)](#) reported the dynamic *collapse* of gravitating envelopes into a more compact equilibrium. What caused the collapse reported by [Ayliffe et al. \(2012\)](#) and the discrepancies with the results of [Wuchterl \(1991b\)](#) could not be asserted due to the intricate hydrodynamic, chemical and radiative effects involved.

The aim of this paper is to examine the properties of self-gravitating planetary envelopes in the regime of the core-nucleated instability. We use hydrodynamic simulations in models of increasing dimensionality, keeping simple assumptions for the thermodynamics of the gas. In particular, *we do not* model the runaway cooling, contraction and accretion of radiative envelopes. After examining the response of one-dimensional envelopes at the critical core mass, we consider departures from spherical symmetry by progressively including the rotation and the shear of the flow around the planet. As a number of studies have already characterized three-dimensional non-gravitating envelopes (e.g., [Bate et al. 2003](#); [Machida et al. 2010](#); [Fung et al. 2015](#)), we focus on the effects induced by the gas gravity on the flow near the core.

We explicit our model and the methods used throughout this paper in Sect. 2. We consider one-dimensional envelopes in Sect. 3, with hydrostatic calculations followed by hydrodynamic simulations. In Sect. 4 we consider rotating envelopes within a two-dimensional axisymmetric model. The differential rotation of the circumstellar disk is introduced in Sect. 5, where we present three-dimensional simulations of embedded planets in the shearing-sheet approximation. We compare these models against previous studies and discuss their implications in Sect. 6.

2 MODEL AND METHODS

We consider a solid planetary core embedded in a circumstellar disk and massive enough to capture its own atmosphere. If m_c is the mass of the core and c_s the isothermal sound speed of the gas, then the Bondi radius $r_B \equiv Gm_c/c_s^2$ is larger than the radius r_c of the core. For simplicity, we consider that the core orbits its star on a circular trajectory, unaffected by the gas drag ([Weidenschilling 1977](#)) or other causes of radial migration ([Kley & Nelson 2012](#)). We consider time intervals of a few tens of orbital periods at most. The properties of the core are fixed and we focus on the dynamics of the gas surrounding it.

2.1 Governing equations

The gas evolves according to the following equations of mass and momentum conservation:

$$\partial_t \rho + \nabla \cdot [\rho \mathbf{v}] = 0, \quad (1)$$

$$\partial_t [\rho \mathbf{v}] + \nabla \cdot [\rho \mathbf{v} \otimes \mathbf{v} + P] = -\rho \nabla \Phi - 2\rho \boldsymbol{\Omega} \times \mathbf{v}, \quad (2)$$

where ρ is the gas density, \mathbf{v} its velocity and P its pressure. The last term of (2) represents the Coriolis acceleration, which we include only when following the core in a frame rotating at the angular frequency $\boldsymbol{\Omega}$. We consider isothermal envelopes in most of this paper, having a pressure $P = \rho c_s^2$

with a single sound speed (temperature) in the entire flow. For a given core mass and disk temperature, the isothermal envelopes are the most massive ones, helping us identify the influence of the gas gravity on the flow. We also consider polytropic envelopes in Sect. 3, for which the equation of state is $P = \kappa \rho^\gamma$ and the isothermal limit corresponds to $\gamma = 1$.

We decompose the gravitational potential Φ as a sum of potentials from the star, the core and the gas. Given the core mass m_c , the potential of the core depends on the radius r as $\Phi_c(r) = -Gm_c/r$. To avoid more complications, we neglect the gravity of the circumstellar disk: in the limit of $\Phi_c \rightarrow 0$ (no core), we require the potential of the gas to be constant. The potential of the gas must therefore satisfy Poisson's equation

$$\Delta \Phi_g = 4\pi G \rho', \quad (3)$$

in which the source term ρ' is the density deviation from its background value ρ_∞ . With this source term, an envelope of constant density ρ_∞ remains gravitationally stable regardless of its size. If the gas density increases near the core, one can define the Jeans length scale $\ell_J^2 \equiv \pi c_s^2 / G \rho'$ beyond which the gas is unstable to gravito-acoustic perturbations ([Jeans 1902](#)).

2.2 Pluto simulations

We performed self-gravitating hydrodynamic simulations using a modified version of the PLUTO 4.0 code ([Mignone et al. 2007](#)). Although the exact numerical setup changes from Sect. 3 to Sect. 5, the integration scheme remains the same for consistency.

We use PLUTO to integrate (1)-(2) in time via a finite-volume method and an explicit second-order Runge-Kutta time-stepping. At the volume interfaces, we use a linear reconstruction with the slope limiter of [Van Leer \(1979\)](#) to estimate the primitive variables (ρ, v) . We then use the approximate Riemann solver of [Roe \(1981\)](#) to compute the interface fluxes. Where the gas pressure varies by more than a factor 5 between adjacent cells, we revert to the more diffusive MINMOD slope limiter ([Roe 1986](#)) and HLL Riemann solver ([Van Leer 1997](#)). When including the Coriolis acceleration, the momentum equations is evolved in a rotating frame so as to conserve angular momentum ([Kley 1998](#); [Mignone et al. 2012](#)).

We include gravity via its potential Φ . We use the Poisson solver described in Appendix B of [Béthune & Rafikov \(2019a\)](#) to obtain the potential of the gas satisfying (3). We always impose $\partial_r \Phi_g = 0$ at the surface of the core, consistently with the absence of gas inside $r \leq r_c$. To avoid a spurious drag arising if the potential lags behind the mass, the Poisson problem is solved at the beginning of every time step. For a spherically symmetric density distribution, the gravitational acceleration $-\partial_r \Phi_g$ could be directly obtained by radial integration of the gas mass. Regardless, we use the same Poisson solver in every dimension for consistency. The numerical error in estimating $\Delta \Phi_g$ is examined in Appendix A.

2.3 Units and conventions

We call envelope the region where the core gravity induces a substantial density accumulation $\rho'/\rho_\infty \gtrsim 1$. Oppositely, background refers to the conditions in the midplane of the circumstellar disk, near the orbital radius of the core but away from the direct influence of the core. The gravitational constant is set to $G = 1$ and we take the radius of the core r_c as distance unit. We use 1D, 2D and 3D in place of one, two and three-dimensional respectively.

3 ONE-DIMENSIONAL ENVELOPES

3.1 1D spherical envelope model

In this section, we examine the 1D radial structure of spherically-symmetric envelopes. We neglect the orbital motion of the planet around its star, as well as the rotation of the envelope around the core. The only forces involved are the pressure support of the gas against gravity. Were an equilibrium to exist, these two forces would balance each other. We focus on the influence of the gas gravity on such hydrostatic equilibria and their stability.

Given the background sound speed c_s of the gas, we measure the mass of the core via its Bondi radius r_B . We measure the background density ρ_∞ relative to the average core density $\rho_c = m_c / \frac{4}{3}\pi r_c^3$. In the limit $\rho_\infty/\rho_c \rightarrow 0$, the gravity of the gas should become negligible compared to the gravity of the core for a finite-sized envelope.

3.2 Semi-analytical solutions

3.2.1 Equations

We design a 1D solver for self-gravitating hydrostatic equilibria. Using a polytropic equation of state $P = \kappa\rho^\gamma$, we rewrite the equation of mass (1) and momentum (2) conservation as

$$\frac{dm}{dr} - 4\pi r^2 [\rho(r) - \rho_\infty] = 0, \quad (4)$$

$$\frac{d \log \rho}{d \log r} + \frac{\rho^{1-\gamma} m(r)}{\gamma \kappa r} = 0, \quad (5)$$

where $m(r)$ is the mass contained inside the sphere of radius r — core and density deviations. One natural boundary condition is $m(r_c) = m_c$. We prescribe the second boundary condition at an arbitrary radius r_{out} and vary the value of r_{out} so as to simulate the influence of the background density and pressure on the envelope. We impose $\rho(r_{\text{out}}) = \rho_\infty$, and set the background sound speed such that $P(r_{\text{out}}) = \rho(r_{\text{out}})c_s^2$ whether $\gamma = 1$ (isothermal) or not.

A solution of interest is readily found in the isothermal non-gravitating case. In this limit, (5) reduces to $d \log \rho / d \log r + r_B/r = 0$, yielding the non-gravitating solution

$$\rho_0(r) = \rho_\infty \exp \left[\frac{r_B}{r} - \frac{r_B}{r_{\text{out}}} \right]. \quad (6)$$

3.2.2 Numerical solutions

We use a Levenberg-Marquardt root finder to solve (4)-(5) with the above boundary conditions as a boundary value

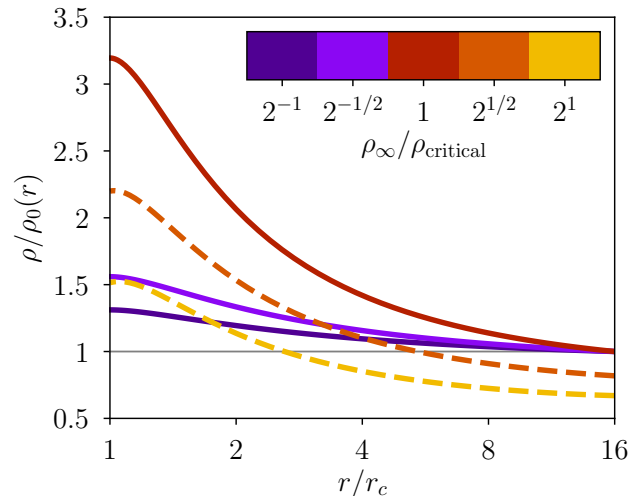


Figure 1. Radial density profile normalized by the non-gravitating solution (6) for $\gamma = 1$, $r_B/r_c = 8$, $r_{\text{out}}/r_c = 16$, and varying the background density ρ_∞ . The dashed curves are obtained when trying to impose $\rho_\infty > \rho_{\text{critical}}$; they satisfy (4)-(5) but not the required outer boundary condition.

problem for $(m, \log \rho)$. The differentiation operators are constructed via a Chebyshev collocation grid on $\log(r)$. With 16 collocation points, the residual error of (4)-(5) is less than 10^{-12} for smooth solutions; we use 64 collocation points by default.

Fig. 1 shows the results of the root finder for $\gamma = 1$, $r_{\text{out}}/r_c = 16$, $r_B/r_c = 8$, and different values of the background density ρ_∞ . In the non-gravitating limit $\rho_\infty \rightarrow 0$ (darker, violet lines), the solution converges to (6). As ρ_∞ increases, the gas gravity becomes significant and adds up to the core gravity. To maintain a hydrostatic equilibrium, the pressure (density) profile becomes progressively steeper. Eventually, we reach a critical value ρ_{critical} beyond which there is no *valid solution* of (4)-(5) satisfying $\rho(r_{\text{out}}) = \rho_\infty$ (lighter, orange curves). We identify this transition by monitoring the error $\rho(r_{\text{out}}) - \rho_\infty$, which suddenly jumps at the threshold $\rho_\infty = \rho_{\text{critical}}$.

Although the outer boundary condition is not satisfied anymore, the density profiles in the regime $\rho_\infty > \rho_{\text{critical}}$ are still solution to (4)-(5) to per cent accuracy over the radial domain. The critical density marks the transition to the second solution branch identified by Perri & Cameron (1974), albeit with a different parametrization. We examine the linear stability of these solutions in Appendix C, and now delimit the domain of existence of solutions satisfying $\rho(r_{\text{out}}) = \rho_\infty$ in our parameter space.

3.3 Critical envelopes

We solve (4)-(5) for various input parameters and track the threshold value ρ_{critical} . We prescribe the outer radius $r_{\text{out}}/r_c \in [16, 64]$ to represent the sphere of influence of a massive embedded core, i.e. roughly one pressure scale of the disk in radius (see Sect. 5.2 and Béthune & Rafikov 2019b). We also prescribe the polytropic exponent γ while

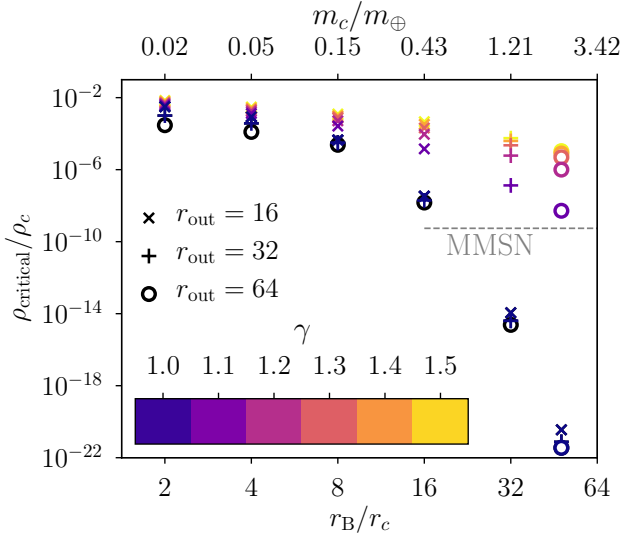


Figure 2. Critical background density relative to the core density for different values of the Bondi radius r_B (*abscissa*), outer radius r_{out}/r_c (*markers*, see legend) and polytropic exponent γ (*colors scale*). Valid solutions are found below the markers, i.e. for smaller ρ_∞/ρ_c . The top axis indicates the corresponding core mass in Earth mass units, assuming that the core has the same density as the Earth and is located at 1 au around a solar-mass star in a disk with aspect ratio $h/r = 0.05$. The dashed horizontal line marks the corresponding MMSN midplane density $\rho \approx 3 \times 10^{-9} \text{ g cm}^{-3}$.

maintaining¹ the background temperature $P(r_{\text{out}}) = \rho_\infty c_s^2$, and the mass of the core via its Bondi radius r_B . We then increase the background density ρ_∞ until the outer boundary condition can no longer be satisfied. The corresponding ρ_{critical} are marked on Fig. 2 relative to the core density ρ_c .

The ratios of $\rho_{\text{critical}}/\rho_c$ marked on Fig. 2 delimit the region of existence of valid solutions from above. With r_c as our distance unit, the core mass is directly $m_c \sim (4/3)\pi\rho_c$. For a given core mass, valid equilibria require a background density ρ_∞ smaller than ρ_{critical} . Reciprocally, solutions satisfying $\rho_\infty = \rho_{\text{critical}}$ can only be found for cores more massive than indicated.

We note three trends on Fig. 2. First, when the mass of the core increases (from left to right), the critical gas-to-core density ratio decreases. Second, increasing the polytropic exponent γ from 1 to 3/2 (lighter markers) allows equilibria at larger background densities. Third, the threshold $\rho_{\text{critical}}/\rho_c$ only slightly decreases with the location of the outer boundary condition r_{out} (marker symbols).

The thresholds obtained by this method agree with those of Sasaki (1989) in the appropriate regime. The critical density drops by orders of magnitude as soon as $r_B/r_c \gtrsim 8$. It falls below the Minimum Mass Solar Nebula (MMSN, Hayashi 1981) midplane density for isothermal envelopes around cores of a few Earth masses at 1 au. However, valid equilibria with $\gamma = 7/5$ still exist for much more massive cores $\gtrsim 10^3 m_\oplus$. Whether the critical density threshold is re-

alistically accessible for more sophisticated thermodynamic structures is outside the scope of this paper.

Having delimited the range of parameters for which valid hydrostatic equilibria exist, we proceed to examine the dynamical reaction of the envelope when the control parameters vary continuously across this limit.

3.4 Direct numerical simulations

3.4.1 Numerical setup

We use the PLUTO code as described in Sect. 2.2 to evolve the density ρ and radial velocity v_r in time for an isothermal gas in 1D spherical geometry. We mesh the radial interval $r/r_c \in [1, 16]$ with 512 logarithmically spaced grid cells. We prevent mass and momentum fluxes through the surface of the core via $(\rho, v_r, \Phi_c)(r_c - \epsilon) = (+\rho, -v_r, +\Phi_c)(r_c + \epsilon)$. At the outer radial boundary, we impose a constant density ρ_∞ and allow the gas to flow in by a linear extrapolation of the radial velocity. The outer boundary condition $\Phi_g(r_{\text{out}}) = 0$ sets a reference value for the gravitational potential of the gas. We initialize the computational domain with a flat density $\rho = \rho_\infty$ and zero velocity. We take the sound speed as velocity unit ($c_s = 1$). The mass of the core is progressively increased from zero to its nominal value, so that the envelope mass builds up in quasi-static equilibrium at every instant.

3.4.2 Non-gravitating limit

When neglecting the gas gravity, the density profile should converge toward (6) given an outer density ρ_∞ and a Bondi radius r_B . We increase the Bondi radius of the core linearly in time from zero up to $16 r_c$ over a time interval of $t_B = 12800 r_c/c_s$, after which it remains equal to $16 r_c$. The resulting density distribution is represented on Fig. 3 as a function of radius and time.

As the Bondi radius of the core increases (from left to right), an inflow of gas through the outer radial boundary allows the density to increase inside the domain. At $c_s t/r_c \approx 12000$ and $r/r_c \approx 8$, the inflow becomes supersonic (cyan contour) and shocks on the inner parts of the envelope. The shock front propagates inward until t_B , i.e., while the mass of the core is still increasing. For $t > t_B$, the shock front propagates outward until the two sonic points merge. After this instant, the envelope sustains acoustic oscillations but matches the analytical solution (6) to 5 per cent accuracy upon time-averaging.

The shock appearing in this simulation is a consequence of the inflow velocity exceeding the sound speed. It implies that the envelope is not in quasi-static equilibrium as intended, certainly because the Bondi radius of the core initially increases too fast. However, the envelope is able to reach a stable equilibrium after the core mass stops increasing.

3.4.3 Self-gravitating envelope

We repeat the same simulation as above, but now including the gravity of the gas. For a Bondi radius $r_B = 16 r_c$, the critical density is $\rho_{\text{critical}}/\rho_c \approx 3.346 \times 10^{-8}$. We impose a slightly larger density $\rho_\infty \approx 3.356 \times 10^{-8} \rho_c$. When the Bondi radius

¹ For static equilibria, one can arbitrarily choose c_s and adjust the core mass according to $m_c = c_s^2 r_B/G$.

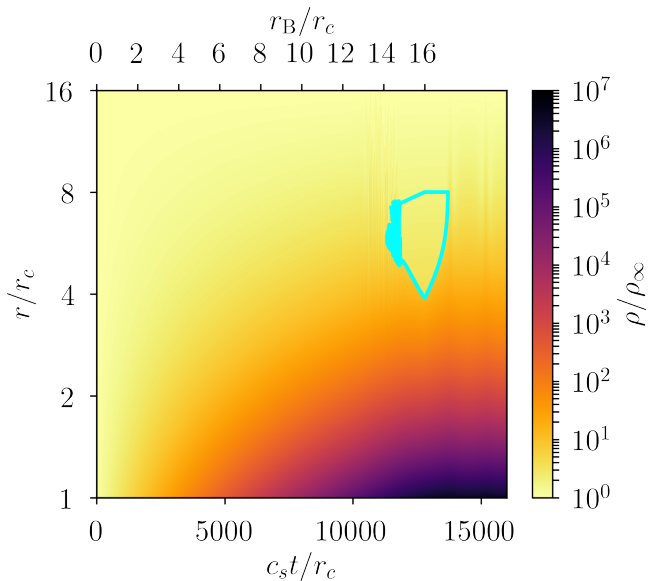


Figure 3. Space-time distribution of the density ρ/ρ_∞ in a non-gravitating envelope. The core mass increases from zero to $r_B = 16r_c$ over the first $t_B = 12800r_c/c_s$ (top axis) after which it is constant. The cyan contour marks the sonic surface $v_r = -c_s$, corresponding to a smooth transonic point (upper part) and a shock (lower part).

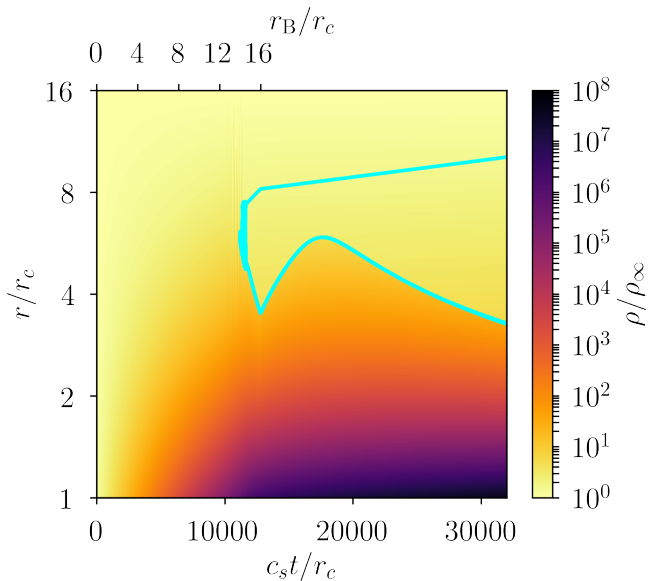


Figure 4. Same as Fig. 3 but including the gas gravity, with a background density larger than its critical value. The inflow remains transonic after the Bondi radius has reached $r_B = 16r_c$; the envelope is then delimited by an inward moving shock front (lower part of the cyan contour).

of the core reaches $16r_c$, no hydrostatic equilibrium should be able to satisfy the outer boundary condition anymore.

The evolution of the self-gravitating density distribution is shown on Fig. 4. As previously, the inflow becomes supersonic before the Bondi radius of the core reaches $16r_c$. After $t_B = 12800r_c/c_s$, the shock moves outward for about

$5 \times 10^3 r_c/c_s$ before starting to move toward the core. The smooth sonic point (upper part of the cyan line) keeps moving outward, meaning that the inflow becomes progressively faster at a given radius. As the two sonic points drift away from one another, the core and its envelope always drive a transonic inflow.

The key difference with the non-gravitating case is that the envelope does not converge to a steady state when ρ_∞/ρ_c exceeds the threshold delimited on Fig. 2. When crossing this threshold, the outer parts of the envelope collapse in near free-fall. As soon as the infalling gas becomes supersonic, it has to shock on the inner parts of the envelope, dissipating momentum and allowing the accumulation of mass.

We verified via simulations at lower core mass (lower dr_B/dt while the core mass is initially increased) and larger ρ_∞ that the collapse precisely occurs at the critical values predicted in Sect. 3.3. However, in this regime the inflow shocks closer to the core and the shocked envelope becomes spatially under-resolved. We verified that a collapse also happens in adiabatic envelopes when crossing the threshold marked on Fig. 2. In this case, adiabatic heating and momentum dissipation at the shock lead to higher pressures in the contracting gas. For $\gamma = 3/2$, $r_{\text{out}}/r_c = 16$ and $r_B/r_c = 16$, the smooth sonic point settles at the outer radius r_{out} and the shock propagates *outward* until the space between the shock and r_{out} is under-resolved. Because these cases are sensitive to the finite extent and resolution of our computational domain, we discuss what governs the dynamics of the envelope in the next section.

3.5 Discussion of 1D models

3.5.1 The core-nucleated instability

By progressively increasing the mass of the core at a fixed ρ_∞ , we have followed the ‘stable’ solution branch for the envelope up to the critical core mass. Beyond this point, the equilibria from the second solution branch (as drawn on Fig. 1 for $\rho_\infty > \rho_{\text{critical}}$) should be linearly unstable (Perri & Cameron 1974; Mizuno et al. 1978; Wuchterl 1990). Due to the sudden collapse of the outer envelope at the critical mass, these equilibria seem inaccessible unless taking them as initial condition (as done by Wuchterl 1991b). We will therefore focus on the non-linear dynamics of the envelope when it crosses the critical mass from below.

It is possible to interpret the trends of Fig. 2 in the non-gravitating limit, assuming that the threshold mainly depends on the envelope mass relative to the core mass (Sasaki 1989). First, the mass of the envelope increases faster than the mass of the core, so gas gravity effects appear at lower background densities ρ_∞ when the mass of the core increases. Second, if the gas pressure varies as ρ^γ , then one can satisfy $\partial_r P = -\rho \partial_r \Phi_c$ with a shallower density profile when increasing γ . To reach the same envelope mass, the background density must then be larger. Third, the envelope mass increases with r_{out} , so it becomes comparable to the core mass at a lower ρ_{critical} when r_{out} increases.

As we show on Fig. 2 and in Appendix C, the absence of global equilibria beyond a critical mass is independent of the gas thermodynamics, which only affect the value of this critical mass. Unlike the instability of a homogeneous gas ball (Ebert 1955; Bonnor 1956), the envelope collapse can

spontaneously stop even though $\gamma < 4/3$ (see Fig. 4). As apparent from the slow propagation of the shock front on Fig. 4, the shocked envelope maintains a nearly hydrostatic equilibrium. Using the method described in Sect. 3.2, we verified that hydrostatic equilibria can indeed be found between the core and the shock, given the post-shock density as an outer boundary condition. In this sense, planetary cores above the critical mass can still support a hydrostatic envelope. We explain below how the extent of this envelope is determined by the ambient conditions.

3.5.2 Long-term evolution

In 1D, if the infalling gas becomes supersonic, then it has to shock before reaching the surface of the core (where $v_r = 0$). The conditions just upstream of the shock are controlled by the ambient (outer boundary) conditions on (ρ, v_r) and by the planet mass. Given the ambient conditions, it is possible to predict the dynamics of 1D envelopes to some extent.

Let $\zeta(t)$ denote the radius of the shock front, u_r the gas velocity in the frame of the shock, and the exponents (u) and (d) identify the upstream and downstream regions respectively. The velocity of the shock is obtained by changing frame: $d\zeta/dt = v_r^{(d)} - u_r^{(d)}$. If the post-shock envelope was exactly hydrostatic ($v_r^{(d)} = 0$), then $d\zeta/dt > 0$ and the shock would propagate outward. The opposite orientation $d\zeta/dt < 0$ on Fig. 4 reveals that the post-shock envelope is contracting ($v_r^{(d)} < 0$). This contraction is due in part to the inward momentum flux, most of it being converted into pressure at the shock. Simultaneously, the accumulation of mass causes the gas potential Φ_g to deepen over time, so the envelope contracts to support its own increasing gravity.

The momentum flux is relevant to locate the shock front. The velocity drop at the shock — $u_r^{(d)}/c_s = c_s/u_r^{(u)}$ in the isothermal case — leads to a large drop in ram pressure ρu_r^2 . The shock ultimately settles where the downstream thermal pressure balances the upstream ram pressure: $\rho^{(d)}c_s^2 \simeq \rho^{(u)}u_r^{(u)2}$. Since the shocked envelope is nearly hydrostatic, $\rho^{(d)}$ decreases radially, so a larger upstream ram pressure would push the shock closer to the core. This is expected if the background density or the accumulated envelope mass increases (as on Fig. 4).

If the ambient density were to decrease, then the shocked shell would expand until the momentum balance condition is satisfied again. If the shock radius ζ extends further than the gravitational radius $Gm(\zeta)/c_s^2$ or the Hill radius of the planet, then the outer parts of the envelope could escape the core by evaporation or gravitational tides. According to this 1D model, a planet may therefore experience a phase of rapid gas accretion only to lose its outer envelope later during the dispersal of the protoplanetary disk.

4 TWO-DIMENSIONAL ENVELOPES

The previous 1D model omits the angular momentum of the background flow with respect to the core. By conservation of angular momentum, the gas should spin faster as it approaches the core. The centrifugal acceleration can then provide a substantial support against gravity, allowing for much less massive envelopes. In this section, our main goal is to

test whether the core-nucleated instability — and the ensuing accretion phase — can also affect rotationally-supported envelopes.

4.1 2D axisymmetric model

We consider a planetary core orbiting its star at the angular frequency Ω about the z axis of the disk. We adopt a frame centered on the core and rotating along its orbit at the angular frequency Ω ; in this frame, the background flow is steady in time. To make things simpler, we neglect the vertical stratification and the differential rotation of the disk. In the absence of the core, the gas density should be constant and the velocity should be zero in this frame, so rotation only manifests itself through the Coriolis acceleration in (2). If radial motions are brought about by the core, then angular momentum conservation will generate a toroidal velocity in this frame.

Let (r, θ, φ) denote spherical coordinates centered on the core, with $\theta = 0$ along the rotation axis z . Assuming that the flow is axisymmetric ($\partial_\varphi = 0$), we use PLUTO to integrate (1)–(2) for $(\rho, v_r, v_\theta, v_\varphi)$ in the (r, θ) poloidal plane.

The interval in polar angle $\theta \in [0, \pi]$ is uniformly meshed with 256 grid cells. The radial interval $r/r_c \in [1, 32]$ is meshed with 256 logarithmically spaced cells. The radial boundary conditions are the same as in 1D (see Sect. 3.4.1), with the addition of $v_\theta = v_\varphi = 0$. Inside the computational domain, we homogenize the density in the innermost grid shell at every timestep, conserving the total mass in the shell. This operation is intended to prevent unresolved mass concentrations when including the gas gravity. About the polar axis $\theta = 0$, we impose

$$(\rho, v_r, v_\theta, v_\varphi)(r, -\theta) = (+\rho, +v_r, -v_\theta, -v_\varphi)(r, +\theta),$$

and similarly about $\theta = \pi \pm \theta$. We initialize the domain with $\rho = \rho_\infty$ and $\mathbf{v} = 0$, and we increase the mass of the core up to its nominal value linearly over $\Omega t/2\pi = 2$ orbital times. The gas entering the computational domain carries a specific angular momentum depending only on its initial latitude and on the outer radius r_{out} .

4.2 Non-gravitating limit

We start by neglecting the gravity of the gas. We take $\rho_\infty = c_s = 1$ and prescribe the angular frequency $\Omega r_c/c_s = 1/32$ of the core around the star. If the vertical stratification of the disk was accounted for, the density would vary over a pressure scale height $h \equiv c_s/\Omega$. The ratio $\Omega r_c/c_s$ would then measure the size of the core relative to the stratification scale of the disk. Typical values of this ratio for super-Earths can be found in section 2.1 of Béthune & Rafikov (2019a). A ratio of $h/r_c = 32$ is arguably reasonable for massive planets at small orbital separations, but under-estimated otherwise. Larger values of h/r_c would place stronger constraints on the explicit integration time steps and therefore be computationally more demanding. We consider two cases with different core masses: $r_B/r_c = 8$ and 16.

4.2.1 Flow structure

Fig. 5 shows the time-averaged flow in the non-gravitating simulation with $r_B/r_c = 16$. In the midplane, the toroidal

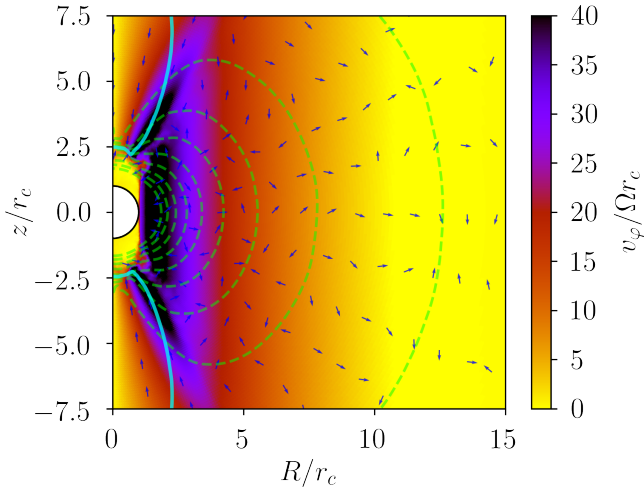


Figure 5. Toroidal velocity (color map), poloidal mass flux (blue arrows, orientation only), mass density (dashed green contours) and sonic surface for the poloidal velocity (solid cyan contours) after time-averaging over $20\Omega^{-1}$ in the simulation with $r_B/r_c = 16$. Note the non-rotating shell directly on top of the core.

velocity increases inward, as expected from angular momentum conservation (Miki 1982; Ormel et al. 2015a). To quantify the level of rotational support, one can convert to Keplerian velocity units

$$\frac{v_\phi}{v_K} = \frac{\Omega r_c}{\sqrt{c_s^2 r_B/R}} \frac{v_\phi}{\Omega r_c} = \frac{1}{32} \sqrt{\frac{R}{r_B}} \frac{v_\phi}{\Omega r_c}. \quad (7)$$

The toroidal velocity increases from $0.2v_K$ at $R = 6r_c$ to its maximum $0.4v_K$ at $R = 2r_c$ in the midplane. Since the centrifugal acceleration scales as v_ϕ^2 , this corresponds to roughly 4 to 16 per cent of rotational support against gravity.

Close to the polar axis, the gas comes with essentially no angular momentum, so only the pressure gradient can balance gravity. However, the envelope does not settle in a static 1D equilibrium. Instead, the gas circulates from high latitudes down to the core and away from the core in the midplane. The inflow become supersonic at $|z| \approx 7r_c$, and subsonic again through a shock at $|z| \approx 2.5r_c$. Averaging the turbulent fluctuations out, the radius of the shock increases by less than $0.2r_c$ over 3000 sound crossing times. With respect to the core, the shock front is therefore stationary over the time scales considered, and it dissipates the momentum of the infalling gas. Downstream of the shocks, the gas remains sitting on top of the core with essentially no momentum.

Whether an accretion shock forms relies on the inflow becoming supersonic. Otherwise, the envelope can be recycled by the poloidal circulation with no net mass accretion onto the core (Ormel et al. 2015b; Béthune & Rafikov 2019b). We now characterize the mass flux through the envelope for different core masses.

4.2.2 Gas accretion and recycling

Let $\bar{X}(r)$ denote the average of X over the sphere of radius r . From the net mass flux $\overline{\rho v_r}$, we define the recycling mass

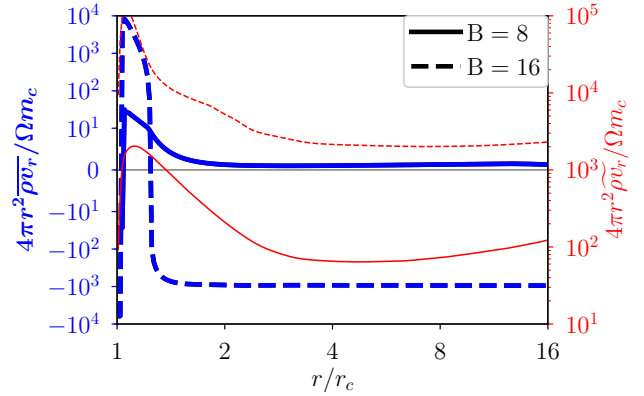


Figure 6. Radial profiles of the net mass flux $\overline{\rho v_r}$ (thick blue, left axis) and recycling mass flux $\overline{\rho v_r}$ (thin red, right axis) averaged over $50\Omega^{-1}$ in non-gravitating 2D simulations with $r_B/r_c = 8$ (solid) and 16 (dashed).

flux $\overline{\rho v_r}$ as the standard deviation $\overline{\rho v_r}^2 \equiv \overline{\rho^2 v_r^2} - \overline{\rho v_r}^2$. The recycling flux is zero when the flow is spherically symmetric, but non-zero if the flow features some degree of circulation.

We draw the radial profiles of the net and recycling mass fluxes in the $r_B/r_c = 8$ and 16 cases on Fig. 6. The recycling flux $\overline{\rho v_r}$ is non-zero in both cases, so both envelopes support a poloidal circulation. The recycling mass flux is maximal closer to the core, and it increases by a factor 10–20 when r_B/r_c increases from 8 to 16. Because of the shell averaging, the recycling flux $\overline{\rho v_r}$ in the $r_B/r_c = 16$ case is non-zero all the way down to the core, although the shocked gas on top of the core does not seem to be efficiently mixed with its surrounding on Fig. 5.

Regarding the net accretion flux $\overline{\rho v_r}$, we obtain two qualitatively different behaviors depending on the core mass. For $r_B/r_c = 16$, the accretion rate $4\pi r^2 \overline{\rho v_r} \approx -10^3 \Omega m_c$ is constant throughout the computational domain. The positive mass flux measured below $1.25r_c$ is most likely a representation artifact due to the different variables used by PLUTO and in the present analysis². We verified that the accretion rate $\partial_t m(r)$ matches the integrated flux $-4\pi r^2 \overline{\rho v_r}(r)$ to better than 10^{-2} relative accuracy, so there is no measurable mass flux through the core boundary.

For $r_B/r_c = 8$, the net mass flux $\overline{\rho v_r}$ drawn on Fig. 6 is compatible with zero through the envelope. The mass cumulated inside the Bondi sphere oscillates by 5 per cent about its equilibrium value, with no net increase over 900 sound crossing times of the Bondi sphere. The absence of mass accretion is related to the absence of dissipative processes, and specifically the absence of accretion shocks. The poloidal velocity is indeed subsonic everywhere in this run, recycling the envelope without accumulating mass on top of the core (Béthune & Rafikov 2019b).

² PLUTO evolves the conservative variables $(\rho, \rho \mathbf{v})$ after reconstruction of the primitive variables (ρ, \mathbf{v}) at the cell interfaces and using the fluxes of the Riemann problem. For our analysis, we estimate the mass flux after time-averaging the cell centered primitive variables.

Table 1. Two-dimensional self-gravitating simulations: label, Bondi radius r_B/r_c , Toomre parameter Q as defined by (8), background density ρ_∞ relative to the core density ρ_c , critical background density for the equivalent 1D setup, and existence of a corresponding 1D hydrostatic equilibrium.

Label	r_B/r_c	Q	ρ_∞/ρ_c	$\rho_{\text{critical}}/\rho_c$	1D static
2B8Q0	8	10^0	6.49×10^{-5}	2.95×10^{-5}	no
2B8Q05	8	$10^{0.5}$	2.05×10^{-5}	2.95×10^{-5}	yes
2B8Q1	8	10^1	6.49×10^{-6}	2.95×10^{-5}	yes
2B16Q1	16	10^1	3.24×10^{-6}	1.10×10^{-8}	no
2B16Q2	16	10^2	3.24×10^{-7}	1.10×10^{-8}	no

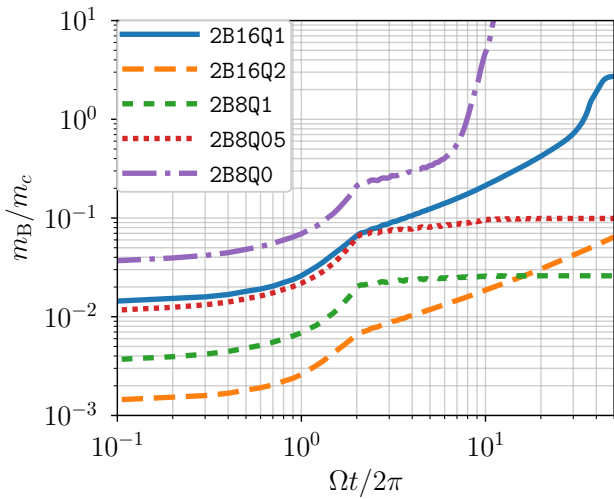


Figure 7. Gas mass m_B contained inside the Bondi sphere of the core relative to the core mass m_c as a function of time for the 2D axisymmetric self-gravitating simulations listed in Table 1. The core mass increases up to its nominal value m_c over the first $\Omega t/2\pi \leq 2$ orbital times.

4.3 Self-gravitating axisymmetric envelopes

We now include the gravity of the gas in addition to rotation. To facilitate comparisons with later 3D results, we adopt $\Omega = 1$ while keeping $\Omega r_c/c_s = 1/32$. For comparison purposes again, we pretend that the planet is embedded in a Keplerian shear flow, and that the disk is stratified over a pressure scale height h . The background density can then be prescribed in terms of the Toomre parameter

$$Q \equiv \frac{\Omega c_s}{\pi G \Sigma} \sim \frac{1}{\pi \sqrt{2\pi} \rho_\infty} \quad (8)$$

with our choice of units. We consider five different combinations of r_B/r_c and Q , as listed in Table 1.

4.3.1 Envelope mass

By comparing the background density ρ_∞ to the critical value ρ_{critical} , one can predict whether hydrostatic equilibria exist in 1D (rightmost column of Table 1). To test whether this prediction holds in 2D, we draw on Fig. 7 the evolution of the gas mass m_B contained inside the Bondi sphere of the core in each self-gravitating 2D simulation.

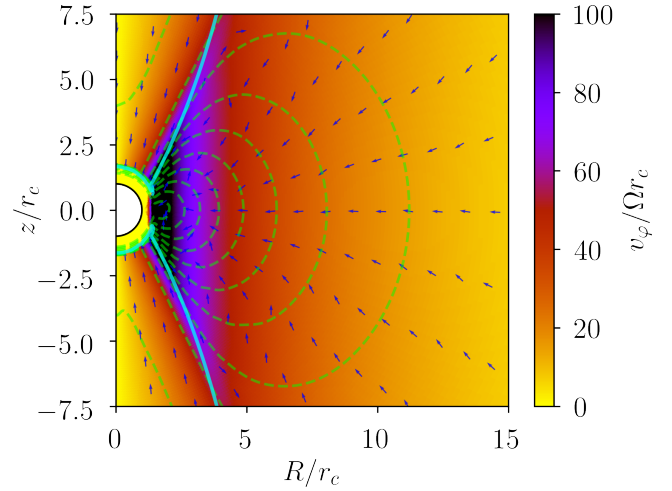


Figure 8. Toroidal velocity (color map), poloidal mass flux (blue arrows, orientation only), mass density (dashed green contour lines) and sonic surface for the poloidal velocity (solid cyan contours) after time-averaging over $10\Omega^{-1}$ in the simulation 2B16Q1.

The parameters of runs 2B8Q05 and 2B8Q1 allow 1D hydrostatic equilibria. In both cases, the Bondi mass m_B converges to a constant value. We can compare it to the envelope mass obtained by integrating the semi-analytic density profiles at $\rho_\infty = \rho_{\text{critical}}$ from r_c to r_B . For $r_B/r_c = 8$ and an outer boundary $r_{\text{out}}/r_c = 32$, the critical Bondi mass is $3.32 \times 10^{-1} m_c$. Both 2B8Q05 and 2B8Q1 indeed converge to a Bondi mass smaller than this critical value.

With its larger background density, the envelope of run 2B8Q0 admits no 1D equilibrium. After increasing the mass of the core over the first two orbital times, the envelope mass keeps increasing. After the Bondi mass reaches $m_B/m_c \approx 0.4$ at $\Omega t/2\pi \approx 6$, the envelope transits to a phase of enhanced mass accretion. The Bondi mass keeps increasing beyond 10 times the final value in run 2B8Q1, and beyond $10^{1/2}$ times the final value in run 2B8Q05. The absence of near-linear scaling of m_B with ρ_∞ indicates that the envelope of run 2B8Q0 does not converge toward an equilibrium. In this case only, we stopped the simulation when $m_B/m_c = 10$.

With a larger core mass, the envelopes of runs 2B16Q1 and 2B16Q2 are also expected to collapse in 1D. The critical Bondi mass is $2.04 \times 10^{-2} m_c$ in this case. Both runs cross this threshold and keep accreting mass until the end of the simulation. In the case of 2B16Q1, we note a change of the slope $\partial_t m_B$ at $\Omega t/2\pi \approx 36$, when the gas mass m_B becomes comparable to the core mass. Whether this transition in accretion rate — and the one observed in run 2B8Q0 — is related to a 1D dynamical collapse is examined in the following section.

4.3.2 From core to gas-dominated envelope

Fig. 8 shows the structure of the flow in run 2B16Q1, averaged over $\Omega t/2\pi \in [30, 35]$. This interval corresponds to the beginning of the enhanced accretion phase on the top right corner of Fig. 7. We verified that the figure does not change qualitatively when averaging later in the simulation. We also

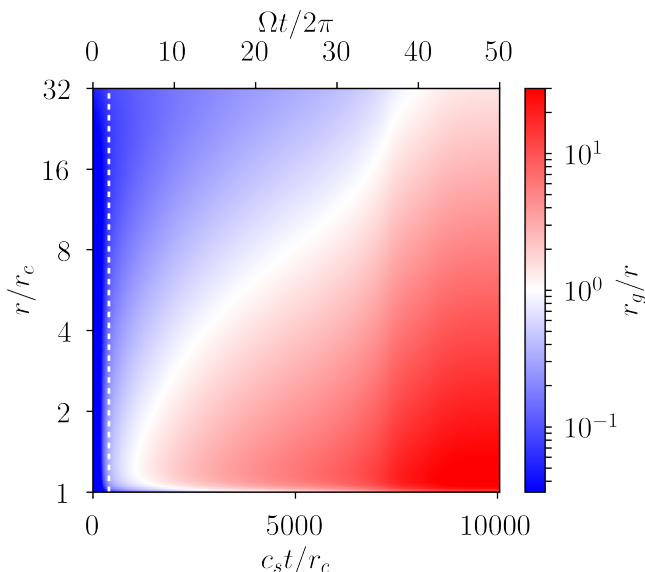


Figure 9. Space-time map of the gas gravitational radius r_g/r as defined by (9) relative to the local radius in run 2B16Q1. The vertical dashed line marks the time $\Omega t/2\pi = 2$ when the core mass is fully set.

obtained a qualitatively similar picture when averaging the flow over the last two orbital times in run 2B8Q0.

As on Fig. 5, the toroidal velocity is larger near the midplane and close to the core. Let $v_g \equiv \sqrt{R\partial_R\Phi}$ denote the toroidal velocity required for fully rotational support in the midplane. The ratio $v_\phi/v_g = 1$ at $1.6r_c$, decreasing to 0.5 at $5.6r_c$ and 0.33 at $9r_c$. With rotation dominating the radial momentum balance, the gas density deviates significantly from a spherical, hydrostatic distribution. The density isocontours form lobes anchored in the midplane at $R \simeq r_c$, delimiting a torus of gas orbiting around the core.

Unlike Fig. 5, the poloidal velocity is converging toward the core in the entire plane of Fig. 8. However, the inflow velocity is supersonic only in the polar accretion cone delimited by the sonic surface. The inflow velocities measured in the midplane remain less than 1 per cent of the sound speed, so this figure does not depict a global collapse on dynamical timescales. As more mass accumulates on the core, the gravitational potential of the gas becomes deeper. The envelope must therefore contract to maintain radial momentum balance in its own gravitational well.

To show the role of the gas gravity more directly, we define the gravitational radius of the cumulative gas mass

$$r_g(r) \equiv \frac{G[m(r) - m_c]}{c_s^2}. \quad (9)$$

Fig. 9 shows the evolution of the gas gravitational radius r_g/r in the simulation run 2B16Q1. At $\Omega t/2\pi \gtrsim 5$, the gravitational radius of the gas encloses the inner parts of the envelope. The gravitational radius increases in time due to mass accretion, reaching the core's Bondi radius $r_g/r_c = 16$ at $\Omega t/2\pi \approx 36$. This time also marks the change of accretion rate on Fig. 7. After $\Omega t/2\pi \gtrsim 40$, the gas is bound and attracted toward the core by its self-gravity mainly.

4.4 Discussion of 2D models

Adding rotation leads to the spontaneous formation of a circulatory flow through the envelope. With the parameter space explored in our isothermal simulations, we find preferentially a polar inflow of gas towards the core and an equatorial outflow. This pattern seems robust to boundary effects since it was reported in three-dimensional simulations including the stratification and differential rotation of the background disk (e.g., Tanigawa et al. 2012; Fung et al. 2015).

In the non-gravitating limit, the polar inflows become supersonic when the Bondi radius of the core $r_B/r_c \gtrsim 16$, in agreement with Béthune & Rafikov (2019b). The supersonic inflows shock on the inner parts of the envelope, dissipating momentum and allowing mass accretion. Given the limited integration time of our simulations, we can only speculate that these envelopes will converge to a steady state (finite mass) on longer time scales, when the polar shocks expand up to the smooth transsonic point as on Fig. 3.

When accounting for the gas gravity, we observe a transition to enhanced gas accretion in runs 2B8Q0 and 2B16Q1, as expected from 1D models. In this phase, the envelope mass can increase without bounds, the accretion rate being only restricted by the available gas at the outer radial boundary. However, the accretion rate over the interval $\Omega t/2\pi \in [2, 20]$ in run 2B16Q1 is still unaffected by the gas gravity. This is apparent from the curve of run 2B16Q2 on Fig. 7, which has the same slope as run 2B16Q1 although it is ten times less massive. When run 2B16Q1 starts accreting at an enhanced rate at $\Omega t/2\pi \approx 36$, the envelope mass exceeds the 1D critical mass by a factor ≈ 40 . The transition to a phase of enhanced accretion instead starts when the gas mass becomes comparable to the core mass.

We do not observe a dynamical collapse of the entire envelope in the 2D simulations of Table 1. Instead, the accretion flow is limited to the polar regions and a rotationally-supported circumplanetary disk forms near the midplane. We do expect a spherical collapse in the non-rotating limit $\Omega r_c/c_s \rightarrow 0$. Even if a fluid element carries a specific angular momentum $l \simeq Rv_\phi$, the acceleration $v_\phi^2/R \simeq l^2/R^3$ alone can balance gravity only up to a limited centrifugal radius. We confirm that a nearly spherical collapse occurs when decreasing Ω below $1/64$ while maintaining $\Omega r_c/c_s = 1/32$ and $r_B/r_c = 16$, i.e., limiting the angular momentum of the gas coming into the computational domain.

5 THREE-DIMENSIONAL ENVELOPES

In both the 1D and 2D models, the runaway (enhanced and unbound) accretion phase is controlled by the outer boundary conditions. In reality, the core has a sphere of influence limited by the tidal potential of the star and by the resulting shear flow of the disk. We now examine this situation via 3D self-gravitating simulations of embedded planetary cores.

5.1 3D model: rotation and shear

Let (x, y, z) be cartesian coordinates centered on the planetary core, with z along its rotation axis, y along its orbital trajectory and x along the star-core radius. We consider a

Table 2. Three-dimensional self-gravitating simulations: label, Bondi radius r_B/r_c , Toomre parameter Q as defined by (8).

Label	r_B/r_c	Q
3B8Q05	8	$10^{0.5}$
3B8Q1	8	10^1
3B16Q1	16	10^1
3B16Q2	16	10^2

small patch of the disk around the core and expand the gravitational potential of the star to second order about the orbital radius of the core (Hill 1878). Assuming that the circumstellar disk is Keplerian (i.e., neglecting radial pressure gradients), the total potential takes the form

$$\Phi = - \underbrace{\frac{3}{2}\Omega^2 x^2}_{\text{star}} - \underbrace{\frac{Gm_c}{r}}_{\text{core}} + \underbrace{\Phi_g}_{\text{gas}}. \quad (10)$$

In this patch of the disk, the Keplerian shear flow induced by the star is $v_y = -(3/2)\Omega x$.

We do not expand the potential of the star in the vertical direction z , i.e., we omit the vertical stratification of the disk. We make this choice to facilitate comparisons with the previous 2D results, and to simply subtract³ a constant value ρ_∞ in the modified Poisson problem (3). This choice is reasonable when the pressure scale height is large compared to the core radius ($h/r_c \gg 1$). We take $\Omega = 1$ and keep $h/r_c = 32$ as in Sect. 4.3.

We extend the computational domain to $(r/r_c, \theta, \varphi) \in [1, 128] \times [0, \pi] \times [0, 2\pi]$. The radial interval is meshed with 128 logarithmically spaced grid cells; the (θ, φ) intervals are meshed with 80×160 uniformly spaced cells. At the outer radius, we impose the initial conditions of a constant density ρ_∞ and a Keplerian shear flow $(v_x, v_y, v_z) = (0, -3\Omega x/2, 0)$. The inner radial boundary conditions are the same as in the 2D setup, including the homogenized density in the innermost grid shell (see Sect. 4.1). The φ boundaries are periodic, and the conditions on the polar axis $\theta = 0$ respect the spherical topology of the domain:

$$[\rho, v_r, v_\theta, v_\varphi](-\theta, \varphi) = [+ \rho, +v_r, -v_\theta, -v_\varphi](\theta, \varphi + \pi)$$

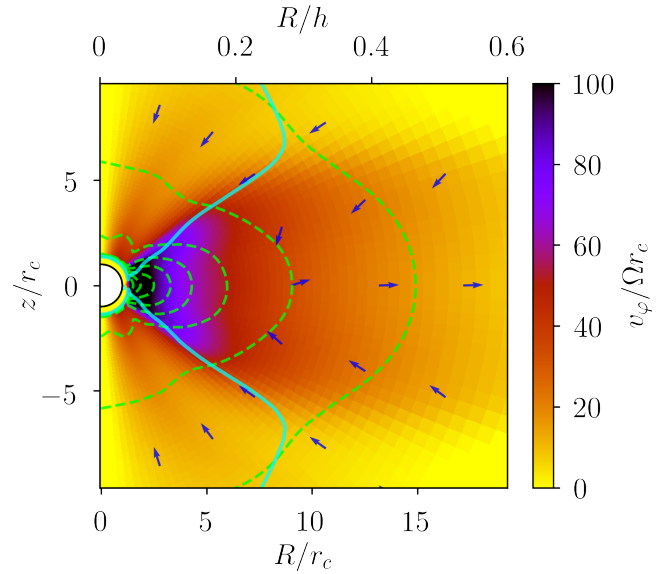
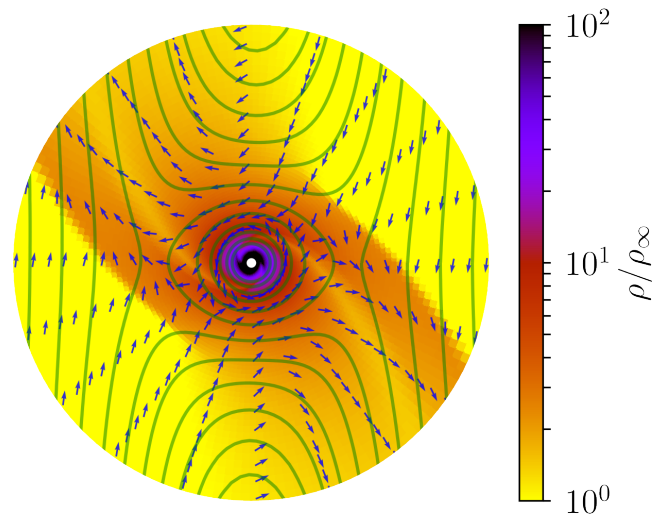
at every radius, and similarly in the opposite hemisphere about $\theta = \pi \pm \theta$. As in Sect. 4, the mass of the core is increased up to its nominal value over the first $\Omega t/2\pi \leq 2$ orbital times.

The two main differences with the numerical setup of Béthune & Rafikov (2019b) are the inclusion of the gas gravity and the omission of the vertical density stratification. The 3D simulations discussed below are listed in Table 2.

5.2 Flow structure

To compare run 3B16Q1 with the equivalent 2D case, we average the flow variables in time over one orbital period $\Omega t/2\pi \in [5.5, 6.5]$ and in the azimuthal (φ) direction, and represent them on Fig. 10. The poloidal mass flux describes a circulatory pattern, with an equatorial outflow and polar inflows shocking close to the core surface. The toroidal

³ Otherwise, one would have to solve the Poisson problem $\Delta\Phi_g = 4\pi G\rho$ for a stratified disk with no planetary core, and then subtract this potential every time the Poisson problem is solved.

**Figure 10.** Same as Fig. 8 in the equivalent 3D case 3B16Q1 after azimuthal and time-averaging over $\Omega t/2\pi \in [5.5, 6.5]$.**Figure 11.** Density ρ/ρ_∞ (color map), velocity (blue arrows, orientation only) and total gravitational potential Φ (green isocontours) after time-averaging over $\Omega t/2\pi \in [5.5, 6.5]$ in the equatorial plane of run 3B16Q1; only the inner $r \leq 2h$ are represented.

velocity reaches $v_\varphi/\Omega r_c \gtrsim 100$ in the midplane inside $R \leq 0.2h = 6.4r_c$. In these inner regions, the density contours form lobes anchored near the surface of the core, delimiting a rotationally-supported circumplanetary disk. One difference with the 2D case of Fig. 8 is the increased opening angle of the accretion cone $\approx 55^\circ$, limiting the rotationally-supported envelope to a smaller range of latitudes near the midplane. Another difference with Fig. 8 is the radially limited extent of the circumplanetary disk: the density iso-contours disjoint from the core are restricted to $R \lesssim 6r_c$.

We show the equatorial flow structure of run 3B16Q1 on Fig. 11. From the isocontours of the gravitational potential,

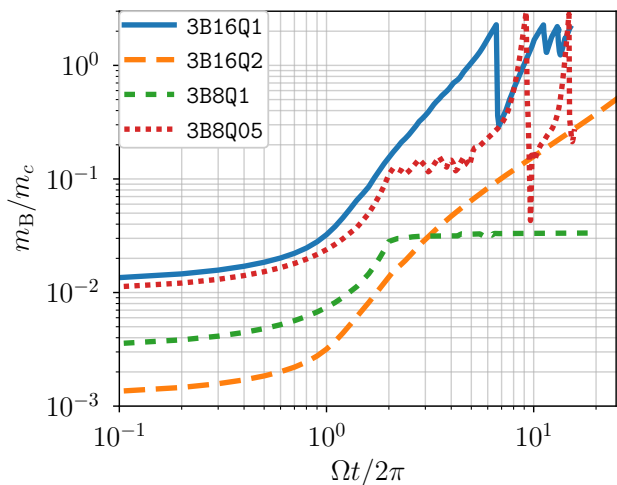


Figure 12. Gas mass contained inside the Bondi sphere of the core relative to the core mass m_c as a function of time for the 3D self-gravitating simulations listed in Table 2. The core mass increases up to its nominal value m_c over the first $\Omega t/2\pi \leq 2$ orbital times.

one can identify the different parts of the flow (see for example Fung et al. 2015). When neglecting the gas gravity, the central region dominated by the potential of the core extends up to the Hill radius $r_H \equiv (Gm_c/3\Omega^2)^{1/3}$. With an envelope mass equal to the core mass at this time (see Fig. 12), the effective Hill radius is only $2^{1/3} \approx 1.26$ larger than in the equivalent non-gravitating case.

Due to the background shear, the envelope is limited to approximately one pressure scale height in radius. At larger distances $|x/h| > 2/3$, the Keplerian shear flow is supersonic with respect to the core; the density perturbations induced by the core are then transported by spiral density waves into the disk. Despite their large spatial extent, we find no significant contribution of the spiral waves to the gravitational potential of the gas, which remains spherically symmetric in good approximation.

5.3 Mass of 3D gravitating envelopes

For each 3D simulation listed in Table 2, we integrate the gas mass m_B contained inside the Bondi radius of the core, normalize it by the final mass m_c of the core, and draw its evolution on Fig. 12.

Only run 3B8Q1 has an envelope mass converging to a finite value. The residual accretion rate is approximately $5 \times 10^{-6} \Omega m_c$, negligible over the duration of the simulation. With a laminar and subsonic poloidal flow (no polar shocks), mass accretion is mainly driven by numerical dissipation in this simulation.

The envelope mass in run 3B16Q2 increases up to 50 per cent of the core mass over the integration time of the simulation. Mass accretion is caused by polar shocks as described in Sect. 5.2. The mass accretion rate increases from $1.9 \times 10^{-2} m_c$ per orbit to $2.6 \times 10^{-2} m_c$ per orbit over the interval $\Omega t/2\pi \in [8, 24]$.

In the last two simulations 3B16Q1 and 3B8Q05, the com-

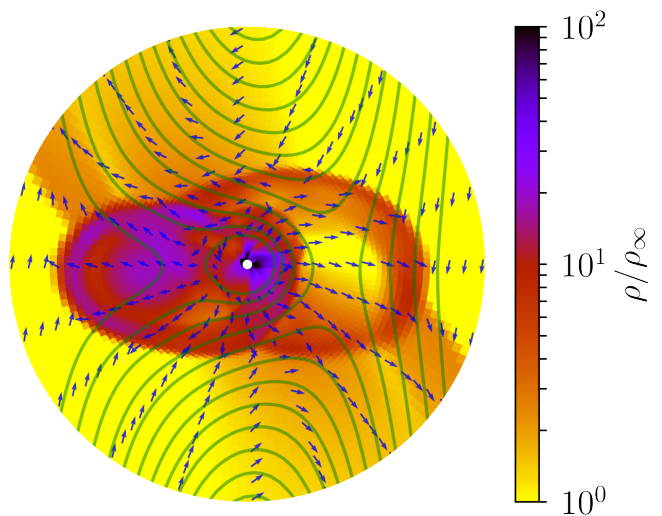


Figure 13. Same as Fig. 11 but at the time $\Omega t/2\pi = 6.7$ in run 3B16Q1, corresponding to the envelope mass drop on Fig. 12.

bination of a large core mass and/or a large background density leads to the most massive envelopes. Both envelopes accrete gas and become as massive as the core during the simulation. However, these envelopes saturate at $m_B/m_c \lesssim 3$. At $\Omega t/2\pi \approx 6.6$ in run 3B16Q1 and 9.5 in run 3B8Q05, the envelope mass drops by an order of magnitude over a fraction of orbital time.

To understand what caused the envelope mass to drop, we show on Fig. 13 a snapshot of the equatorial flow in run 3B16Q1 at $\Omega t/2\pi = 6.7$. The density distribution features two arc-shaped shocks enclosing the core. Inside the bubble delimited by these shocks, the gas moves away from the core at supersonic velocity. The gravitational potential is distorted compared to Fig. 11. The isocontours of potential are pinched toward the core on the left side of Fig. 13, indicating that the blob of gas ejected to the left carries a mass comparable to that of the core.

The envelope of run 3B8Q05 ‘explodes’ in a similar fashion at $\Omega t/2\pi \approx 9.5$. The explosions are preceded by the fragmentation of the gas in the innermost parts of the envelope. The resulting density clumps exert a torque on the surrounding material, throwing most of the envelope mass outside the Hill sphere of the core. To assert whether this fragmentation is caused by Jeans instability, we compute the Jeans length $\ell_J^2 \equiv \pi c_s^2/G\rho'$. In run 3B16Q1 at $\Omega t/2\pi = 6.5$, the shell-averaged Jeans length goes as low as $0.1 r_c$ near the core surface, resolved by only 3 to 5 grid cells. This length is smaller than the extent of the shocked shell $\approx 0.3 r_c$ on Fig. 10, so the envelope could be unstable to radial density perturbations.

We did not observe gravitational fragmentation in the equivalent 2D simulation 2B16Q1. We successfully reproduced the 2D runs 2B16Q1 and 2B8Q05 at a reduced resolution of 96×96 cells over (r, θ) , comparable to the 3D resolution inside $r/r_c \leq 32$. The absence of fragmentation in these low-resolution 2D runs supports that fragmentation is not caused by the lower numerical resolution of our 3D simulations. It also points towards non-axisymmetric disturbances to trigger the envelope fragmentation. Higher resolution 3D

simulations will be required to examine this issue when computational resources allow it.

After the explosion, the remaining envelope is less massive than the core again. The envelope remnant settles as a new hydrostatic shell, and the process of polar mass accretion resumes until the next explosion. This leads to the saturated behavior of the envelope mass with time shown on Fig. 12 for runs 3B16Q1 and 3B8Q05.

6 DISCUSSION

6.1 Comparison with previous works

6.1.1 Non-gravitating envelopes

The 3D simulations are most easily compared with those of Béthune & Rafikov (2019b), who used a nearly identical setup. Comparing run 3B16Q1 with the equivalent non-gravitating run H32B16 (see their Figure 10 (e)), the accretion cones are wider, the inflow becomes supersonic higher above the core, and the density contours are more pinched around the midplane. 3B16Q1 shares more similarities with run H32B32 on Figure 10 (f) of Béthune & Rafikov (2019b), for which the Bondi radius of the core is twice larger ($r_B/r_c = 32$). This is consistent with the fact that the envelope mass equals the core mass at this time in run 3B16Q1, see Fig. 12. In other words, the envelope structure in run 3B16Q1 is the same as if the gas mass was simply added to the core mass. To allow a more quantitative comparison, we reproduce Fig. 10 for the non-gravitating simulation H32B32 of Béthune & Rafikov (2019b) in Appendix B.

We estimate the size of the circumplanetary disk formed in run 3B16Q1 as the radius R_d at which the specific angular momentum Rv_ϕ is maximal. The disk size $R_d \approx 0.32 \times (1.26 r_H)$ is remarkably close to the $r_H/3$ predicted by Quillen & Trilling (1998) after correcting the Hill radius r_H by a factor $2^{1/3}$ for the enclosed gas mass. This ratio is larger than the $r_H/10$ found by Wang et al. (2014) in isothermal simulations around intermediate-mass cores, but it is supported by the radiative simulations of D’Angelo et al. (2003) and Ayliffe & Bate (2009) around high-mass cores.

Because the accretion flow is restricted to the polar cones, the mass accretion rate should be sensitive to the vertical stratification of the disk. Since we omit the disk stratification in the present study, we expect larger accretion rates compared to those of Machida et al. (2010); Béthune & Rafikov (2019b). The accretion rate of $2 \times 10^{-2} m_c$ per orbit in run 3B16Q2 is indeed 10^3 times larger than predicted from equation (13) of Béthune & Rafikov (2019b).

6.1.2 Self-gravitating envelopes

Wuchterl (1991b) presented radiative simulations of 1D envelopes at the critical core mass. He found that the core loses most of its envelope by launching an *outflow*. In our 1D isothermal simulations, the ‘instability’ always develops as an *inflow* toward the core. As discussed in Sect. 3.5 above and in section 3.2 of Wuchterl (1991b), no hydrostatic equilibria connecting the core to the disk can be found beyond the critical mass. Whether the subsequent evolution is a collapse or an expansion of the envelope should therefore be

determined by the outer boundary conditions. In the simulations of Wuchterl (1991b), the critical solution is taken as initial condition, with no initial velocity. In our case, the gas already flows inward when the core reaches the critical mass. This difference could select the inflow as a favored outcome of our setup.

Beyond the critical mass, one can still find hydrostatic equilibria for an isolated planetary envelope. Perri & Cameron (1974), Mizuno et al. (1978) and Wuchterl (1990) found that these equilibria are linearly unstable due to the adiabatic index $\gamma < 4/3$ in the H_2 dissociation region. We confirm the linear instability of these equilibria in Appendix C, where we also find unstable modes for $\gamma > 4/3$. We argue that this linear analysis might not be relevant for embedded planets because of fast reaction (e.g., free-fall of the surrounding disk) happening at the critical mass.

Ayliffe et al. (2012) described the hydrodynamics of gravitating planetary envelopes in 3D radiative simulations. The envelope of their most massive core ($33M_\oplus$ in model J) undergoes a hydrodynamic collapse, after which it settles into a new equilibrium and resumes gas accretion. We do not observe a collapse of the hydrostatic inner envelope in our multi-dimensional simulations, even when they enter an enhanced accretion phase. The sudden contraction of the inner envelope in model J of Ayliffe et al. (2012) might be caused by an opacity drop as the temperature rises near the core, leading to a more isothermal (steeper) density profile.

6.2 From 1D to 3D

In 1D models the radial extent of the envelope must be prescribed a priori. We showed in Sect. 3.3 that the location of this boundary weakly affects the value of the critical mass when $r_B/r_c \geq 8$. In 3D the envelope is limited by the background shear to roughly one pressure scale $h \equiv c_s/\Omega$ around the core. The 2D axisymmetric simulations extending to h should therefore be comparable to the 3D simulations regarding the core-nucleated instability.

From 1D to 2D axisymmetric, we still find a transition to runaway (enhanced and unbound) gas accretion. However, mass accretion is initially driven by transsonic inflows with no role of the gas gravity. The mass accretion rate increases only when the envelope mass becomes comparable to the core mass, which can be orders of magnitude larger than the critical mass predicted in 1D static models. If the mass accretion rate is proportional to the mass of the planet as in non-gravitating simulations (Machida et al. 2010; Béthune & Rafikov 2019b), then the planet mass should increase exponentially in time — as long as the disk can provide this material.

From 2D axisymmetric to 3D, we can compare the evolution of the envelope mass on Fig. 7 and Fig. 12 respectively. The mass accretion rate in run 3B16Q2 is twenty times larger than in the equivalent 2D run 2B16Q2. This is related to the different properties of the background flow. In 2D, the incoming gas has a prescribed angular momentum as if the outer boundary was in solid body rotation. In 3D, the shear flow has a different vorticity distribution (Krumholz et al. 2005), resulting in wider accretion cones and larger accretion rates. Unlike their 2D analogues, the 3D accretion rates of runs 3B16Q1 and 3B16Q2 do not significantly increase when the ratio $m_B/m_c \gtrsim 50$ per cent. The fragmentation of the in-

ner envelope happens before a phase of accelerated growth can be clearly identified.

6.3 Gas thermodynamics

The envelopes presented by [Ayliffe et al. \(2012\)](#) all accrete gas at an accelerating rate when the envelope mass becomes comparable to the core mass (see their Figure 1). The dust opacity — which might vanish in the vicinity of the core ([Podolak 2003](#); [Movshovitz et al. 2010](#)) — controls the efficiency of radiative cooling, and therefore the envelope contraction and accretion (see [Ayliffe et al. 2012](#), Figure 2). If radiative cooling only affects the timescale of mass accretion, e.g., neglecting envelope recycling ([Ormel et al. 2015b](#); [Kurokawa & Tanigawa 2018](#)), then our simulations could be appropriate in late stages of gas accretion onto high-mass cores ($\geq 15 M_{\oplus}$ in model A of [Ayliffe et al. 2012](#)).

The envelope mainly accretes gas through polar inflows, with a negligible contribution from the circumplanetary disk to the mass accretion rate ([Machida et al. 2010](#)). For an isothermal gas, the inflows lose momentum by shocking on the inner envelope. For an adiabatic gas, the momentum would first be converted into heat, which would then have to be radiated away ([Szulágyi et al. 2014](#)). Calculations of the shock radiation efficiency point toward isothermal conditions ([Marleau et al. 2017, 2019](#)). The mass accretion rate parametrized by [Machida et al. \(2010\)](#) and [Béthune & Rafikov \(2019b\)](#) could therefore be used to determine the time required for gas gravity to become important after a supersonic inflow develops.

Regarding the fragmentation of the envelope in runs 3B16Q1 and 3B8Q05 (see Fig. 13), it is made possible by the somewhat unrealistic isothermal equation of state. Isothermal envelopes have the largest mass and the steepest density profile given a background temperature, making them most easily prone to Jeans instability near the core surface. In case of instability, the gravitational collapse would be limited for an adiabatic contraction of the envelope, and eventually regulated by the efficiency of radiative cooling.

7 SUMMARY AND PERSPECTIVES

We studied the hydrodynamics of embedded planetary envelopes in the regime where the gravity of the gaseous envelope becomes comparable to the gravity of the solid core. We focused on isothermal envelopes and considered three models of increasing complexity:

- (i) a 1D model for spherically symmetric envelopes, helping us investigate the nature of the core-nucleated instability through hydrostatic and hydrodynamic calculations;
- (ii) a 2D model for axisymmetric envelopes, allowing a rotationally-supported circumplanetary disks to form by conservation of angular momentum;
- (iii) a 3D model including the tidal potential of the star, where the planetary core is embedded in the differentially rotating circumstellar disk, but omitting the vertical stratification of the disk.

We summarize our main conclusions as follows:

- In spherically-symmetric envelopes, the core-nucleated

instability corresponds to the absence of equilibrium connecting the core to the ambient conditions in the circumstellar disk. The following reaction can be a contraction or an expansion of the envelope until momentum balance is satisfied again.

- Including rotation, the formation of a circumplanetary disk does not prevent the transition to runaway (accelerated and unbound) gas accretion; it only restricts the accretion flow to the polar cones, where the gas has a negligible angular momentum with respect to the core.
- In rotationally-supported envelopes, the accelerated accretion phase starts when the envelope mass becomes comparable to the core mass, irrespective of the critical mass computed in 1D models.
- Because most of an isothermal envelope mass is accumulated at the surface of the core, the flow structure is the same as if the gas mass was simply added to the core mass in a non-gravitating medium. The mass of 3D isothermal envelopes saturate around a few core masses due to fragmentation, preventing their unlimited growth.

The main shortcoming of this study is the extremely simplified treatment of the gas thermodynamics. Future works should address this issue by progressively accounting for radiative energy transport and gas chemistry, expanding the results of [Ayliffe et al. \(2012\)](#). To gain some predictive power, this study should also be repeated by embedding the core within a global disk model. This step is necessary to understand the outcome of runaway gas accretion after the planet opens a gap in the disk ([Ginzburg & Chiang 2019](#)) and the disk eventually disperses ([Alexander et al. 2014](#)).

ACKNOWLEDGEMENTS

Financial support of this work by the Isaac Newton Trust and the Department of Applied Mathematics and Theoretical Physics is gratefully acknowledged. I thank Richard Booth for his early suggestions, and the anonymous referee for his constructive comments that improved the quality of this paper. The results presented here were obtained before the internship of Sabina Sagynbayeva, whom I co-supervised with Roman R. Rafikov on 1D simulations of self-gravitating isothermal envelopes. I thank both of them for helping me develop more lucidity on this topic.

REFERENCES

- ALMA Partnership et al., 2015, *ApJ*, 808, L3
 Alexander R., Pascucci I., Andrews S., Armitage P., Cieza L., 2014, *Protostars and Planets VI*, pp 475–496
 Ayliffe B. A., Bate M. R., 2009, *MNRAS*, 397, 657
 Ayliffe B. A., Laibe G., Price D. J., Bate M. R., 2012, *MNRAS*, 423, 1450
 Bate M. R., Lubow S. H., Ogilvie G. I., Miller K. A., 2003, *MNRAS*, 341, 213
 Béthune W., Rafikov R. R., 2019a, *MNRAS*, 487, 2319
 Béthune W., Rafikov R. R., 2019b, *MNRAS*, 488, 2365
 Birnstiel T., Fang M., Johansen A., 2016, *Space Sci. Rev.*, 205, 41
 Bonnor W. B., 1956, *MNRAS*, 116, 351
 Booth R. A., Clarke C. J., 2019, *MNRAS*, 483, 3718
 Boss A. P., 1998, *ApJ*, 503, 923

Boss A. P., 2000, *ApJ*, **536**, L101
Cameron A. G. W., 1973, *Icarus*, **18**, 407
D'Angelo G., Henning T., Kley W., 2003, *ApJ*, **599**, 548
Dong R., Vorobyov E., Pavlyuchenkov Y., Chiang E., Liu H. B., 2016, *ApJ*, **823**, 141
Ebert R., 1955, *Z. Astrophys.*, **37**, 217
Eisner J. A., Hillenbrand L. A., Carpenter J. M., Wolf S., 2005, *ApJ*, **635**, 396
Forgan D. H., Ilee J. D., Cyganowski C. J., Brogan C. L., Hunter T. R., 2016, *MNRAS*, **463**, 957
Forgan D. H., Ilee J. D., Meru F., 2018, *ApJ*, **860**, L5
Fung J., Artymowicz P., Wu Y., 2015, *ApJ*, **811**, 101
Gammie C. F., 2001, *ApJ*, **553**, 174
Ginzburg S., Chiang E., 2019, *MNRAS*, **487**, 681
Goldreich P., Ward W. R., 1973, *ApJ*, **183**, 1051
Hayashi C., 1981, *Progress of Theoretical Physics Supplement*, **70**, 35
Hayashi C., Nakazawa K., Mizuno H., 1979, *Earth and Planetary Science Letters*, **43**, 22
Hill G. W., 1878, *American journal of Mathematics*, **1**, 5
Ikoma M., Nakazawa K., Emori H., 2000, *ApJ*, **537**, 1013
Ikoma M., Emori H., Nakazawa K., 2001, *ApJ*, **553**, 999
Jeans J. H., 1902, *Philosophical Transactions of the Royal Society of London Series A*, **199**, 1
Kley W., 1998, *A&A*, **338**, L37
Kley W., Nelson R. P., 2012, *ARA&A*, **50**, 211
Krumholz M. R., McKee C. F., Klein R. I., 2005, *ApJ*, **618**, 757
Kurokawa H., Tanigawa T., 2018, *MNRAS*, **479**, 635
Lissauer J. J., Stevenson D. J., 2007, in Reipurth B., Jewitt D., Keil K., eds, *Protostars and Planets V*. p. 591
Liu H. B., et al., 2016, *Science Advances*, **2**, e1500875
Machida M. N., Kokubo E., Inutsuka S.-i., Matsumoto T., 2010, *MNRAS*, **405**, 1227
Marleau G.-D., Klahr H., Kuiper R., Mordasini C., 2017, *ApJ*, **836**, 221
Marleau G.-D., Mordasini C., Kuiper R., 2019, *ApJ*, **881**, 144
Mignone A., Bodo G., Massaglia S., Matsakos T., Tesileanu O., Zanni C., Ferrari A., 2007, *ApJS*, **170**, 228
Mignone A., Flock M., Stute M., Kolb S. M., Muscianisi G., 2012, *A&A*, **545**, A152
Miki S., 1982, *Progress of Theoretical Physics*, **67**, 1053
Mizuno H., 1980, *Progress of Theoretical Physics*, **64**, 544
Mizuno H., Nakazawa K., Hayashi C., 1978, *Progress of Theoretical Physics*, **60**, 699
Movshovitz N., Bodenheimer P., Podolak M., Lissauer J. J., 2010, *Icarus*, **209**, 616
Nimmo F., Kretke K., Ida S., Matsumura S., Kleine T., 2018, *Space Sci. Rev.*, **214**, 101
Ormel C. W., Kuiper R., Shi J.-M., 2015a, *MNRAS*, **446**, 1026
Ormel C. W., Shi J.-M., Kuiper R., 2015b, *MNRAS*, **447**, 3512
Perri F., Cameron A. G. W., 1974, *Icarus*, **22**, 416
Podolak M., 2003, *Icarus*, **165**, 428
Podolak M., Hubbard W. B., Pollack J. B., 1993, in Levy E. H., Lunine J. I., eds, *Protostars and Planets III*. p. 1109
Pollack J. B., Hubickyj O., Bodenheimer P., Lissauer J. J., Podolak M., Greenzweig Y., 1996, *Icarus*, **124**, 62
Quillen A. C., Trilling D. E., 1998, *ApJ*, **508**, 707
Rafikov R. R., 2006, *ApJ*, **648**, 666
Rice W. K. M., Armitage P. J., Bate M. R., Bonnell I. A., 2003, *MNRAS*, **339**, 1025
Roe P., 1981, *Journal of Computational Physics*, **43**, 357
Roe P. L., 1986, *Annual review of fluid mechanics*, **18**, 337
Safronov V. S., 1960, *Annales d'Astrophysique*, **23**, 979
Safronov V. S., 1969, *NASA Tech. Trans.*, pp F-677
Sasaki S., 1989, *A&A*, **215**, 177
Szulágyi J., Morbidelli A., Crida A., Masset F., 2014, *ApJ*, **782**, 65
Tanigawa T., Ohtsuki K., Machida M. N., 2012, *ApJ*, **747**, 47

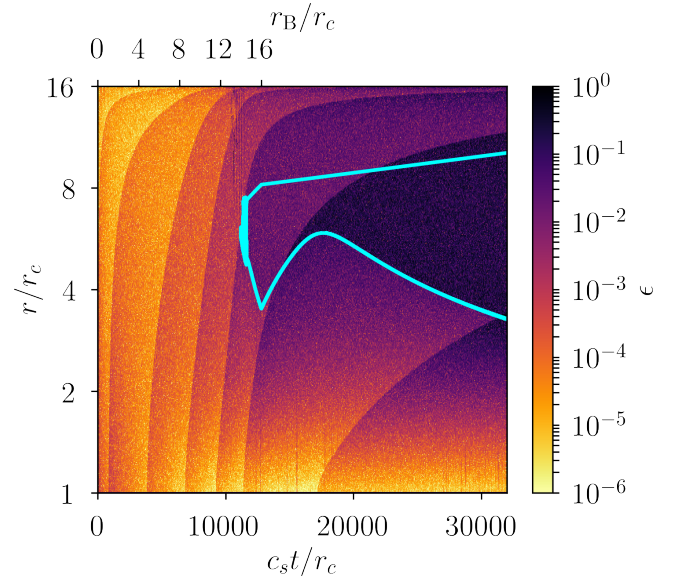


Figure A1. Relative error of the Poisson solver as defined by (A1) in the 1D self-gravitating simulation of Fig. 4. The cyan contour line marks the sonic points $v_r = -c_s$.

Toomre A., 1964, *ApJ*, **139**, 1217
Van Leer B., 1979, *Journal of Computational Physics*, **32**, 101
Van Leer B., 1997, in Hussaini M. Y., Van Leer B., Van Rosendale J., eds, *Upwind and high-Resolution schemes*. Springer, Berlin, Heidelberg, pp 33–52
Wang H.-H., Bu D., Shang H., Gu P.-G., 2014, *ApJ*, **790**, 32
Weidenschilling S. J., 1977, *MNRAS*, **180**, 57
Wuchterl G., 1990, *A&A*, **238**, 83
Wuchterl G., 1991a, *Icarus*, **91**, 39
Wuchterl G., 1991b, *Icarus*, **91**, 53

APPENDIX A: NUMERICAL ACCURACY OF THE POISSON SOLVER

To solve the Poisson problem (3) in PLUTO, we use the parallel solver described in Appendix B of Béthune & Rafikov (2019a). The second-order finite difference discretization of the Laplacian operator might introduce numerical errors when the density distribution becomes steep. To verify that the Poisson solver performs well in the simulations presented above, we compute the error

$$\epsilon \equiv \frac{\Delta\Phi_g}{4\pi G\rho'} - 1 \quad (\text{A1})$$

in the 1D self-gravitating simulation of Fig. 4. With a density contrast of 10^8 , this simulation is our most unfavorable case regarding numerical accuracy.

The error ϵ in this simulation is shown on Fig. A1 as a function of time and radius. The maximal error is less than 10^{-2} before the inflow becomes supersonic, and later between 0.1 and 0.3 upstream of the shock. The absolute error on $\Delta\Phi_g$ is continuous across the shock, so the apparent jump in ϵ only comes from the jump in ρ' . After a shock forms, the Poisson problem is dominated by the innermost regions, where the Laplacian $\Delta\Phi_g$ remains overall resolved to per cent accuracy.

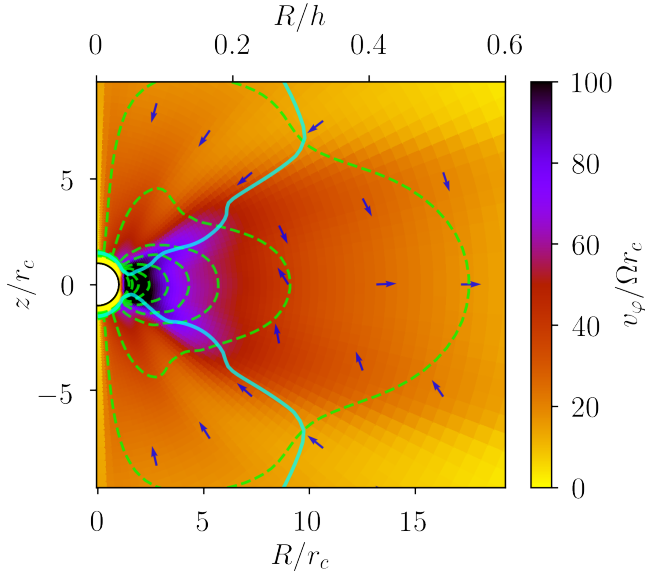


Figure B1. Non-gravitating 3D isothermal simulation H32B32 of Béthune & Rafikov (2019b) with a Bondi radius $r_B/r_c = 32$ and including vertical stratification on a pressure scale $h/r_c = 32$, to be compared with Fig. 10.

APPENDIX B: THREE-DIMENSIONAL NON-GRAVITATING SIMULATION

Fig. B1 shows the time and azimuthally averaged flow structure in run H32B32 of Béthune & Rafikov (2019b). Unlike run 3B16Q1 shown on Fig. 10, this envelope is non-gravitating, the background disk is vertically stratified on a pressure scale $h = 32r_c$, and the core is twice more massive with $r_B = 32r_c$.

In comparison with Fig. 10, the density iso-contours are pinched toward the core near the polar axis. This feature is caused by the low-density polar inflows; it is the only region where the vertical stratification of the disk affects the envelope. Near the midplane, the density iso-contours form lobes with a similar aspect ratio, also delimiting a circumplanetary disk. The toroidal velocity reaches similar amplitudes $v_\phi \lesssim 100\Omega r_c$ in the midplane.

APPENDIX C: LINEAR STABILITY OF SELF-GRAVITATING ENVELOPES

We examine the linear stability of the 1D self-gravitating equilibria obtained in Sect. 3.2. These equilibria represent isolated / unbound planetary envelopes. They cannot satisfy arbitrary condition on ρ away from the core, so they cannot be continuously connected to the ambient disk in general.

We set the outer radius $r_{\text{out}}/r_c = 16$, the Bondi radius $r_B/r_c = 8$, and the background temperature via $P(r_{\text{out}}) = \rho(r_{\text{out}})c_s^2$. Given a polytropic exponent γ , we find the background density beyond which the boundary condition $\rho(r_{\text{out}}) = \rho_\infty$ cannot be satisfied anymore. Beyond this point, we can still parametrize the solutions by their envelope mass $m_g \equiv \int_{r_c}^{r_{\text{out}}} 4\pi r^2 \rho dr$ relative to the mass m_{critical} integrated at the threshold $\rho_\infty = \rho_{\text{critical}}$. With this parametrization, the

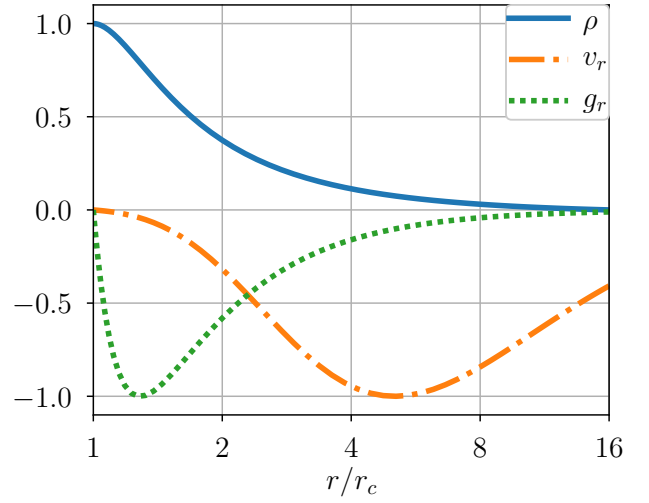


Figure C1. Linearly unstable mode of an isothermal envelope of radius $r_{\text{out}}/r_c = 16$, with a core mass $r_B/r_c = 8$ and an gas mass $m_g = 0.46m_c$, close to the critical value. The corresponding growth rate is $\omega r_c/c_s \approx 1.03 \times 10^{-2}$. Each curve is normalized by its extremal value on the interval.

residual error on the solutions is 10^{-12} even above the critical mass.

Given an equilibrium profile $\bar{\rho}$, the linearized equations for the perturbed density, velocity and gravitational acceleration (ρ', v_r', g_r') for a polytropic gas with $P = \kappa \bar{\rho}^\gamma$ are:

$$\partial_t \rho' = -\frac{1}{r^2} \frac{\partial}{\partial r} \left[r^2 \bar{\rho} v_r' \right], \quad (\text{C1})$$

$$\partial_t v_r' = -\frac{1}{\bar{\rho}} \frac{\partial}{\partial r} \left[\gamma \kappa \bar{\rho}^{\gamma-1} \rho' \right] + \frac{\rho'}{\bar{\rho}^2} \frac{\partial}{\partial r} \left[\kappa \bar{\rho}^\gamma \right] + g_r', \quad (\text{C2})$$

$$\partial_t g_r' = 4\pi \bar{\rho} v_r'. \quad (\text{C3})$$

We look for eigenmodes satisfying $\rho'(r_{\text{out}}) = v_r'(r_c) = g_r'(r_c) = 0$, and with a time dependence $\sim \exp[\omega t]$. We focus on real and positive eigenvalues ω , i.e., unstable modes.

As long as $m_g < m_{\text{critical}}$, the spectrum of (C1)-(C3) is purely imaginary, corresponding to gravito-acoustic oscillations of the envelope at quantized wavelengths. When $m_g \geq m_{\text{critical}}$, the pair of eigenvalues corresponding to the largest-scale modes become real, leading to a contraction of the envelope as illustrated on Fig. C1.

Fig. C2 shows the growth rates $\omega \in \mathbb{R}^+$ obtained when varying the polytropic exponent and the envelope mass. The growth rates are only a fraction of c_s/r_c , i.e. slow compared to the sound-crossing or free-fall time of the envelope. The case with $\gamma = 3/2$ also features unstable modes, with even larger growth rates compared to the $\gamma = 1$ case. In both cases, the growth rate has a maximum as a function of the envelope mass.

We find linearly unstable modes for $\gamma = 3/2$, whereas a homogeneous self-gravitating ball of gas should be linearly stable for $\gamma > 4/3$. The larger growth rates found in the $\gamma = 3/2$ case, as well as the presence of a maximal growth rate can be interpreted from a mean-field point of view. The equilibrium density profile $\bar{\rho}$ become steeper as m_g increases or γ decreases, such that the average Jeans length ℓ_J eventually decreases over the scale r_{out} of the unstable mode.

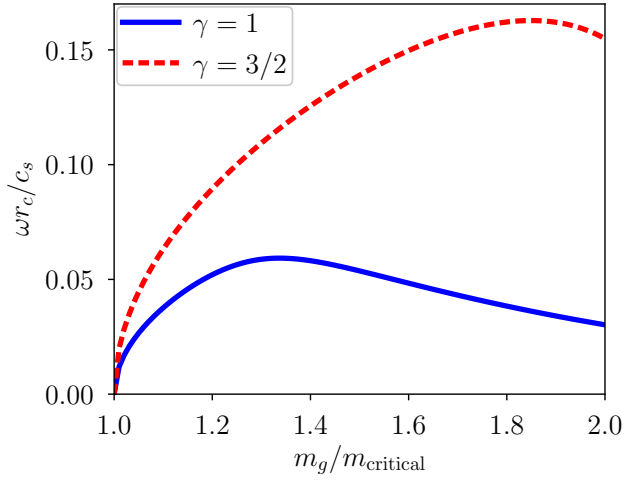


Figure C2. Real eigenvalues from the system (C1)-(C3) as a function of the envelope mass m_g and for different polytropic exponents γ (see legend).

This paper has been typeset from a $\text{\TeX}/\text{\LaTeX}$ file prepared by the author.